Melting and refreezing beneath Roi Baudouin Ice Shelf (East Antarctica) inferred from radar, GPS, and ice core data

Pattyn, F.; Matsuoka, K.; Callens, D.; Conway, H.; Depoorter, M.; Docquier, D.; Hubbard, B.; Samyn, D.; Tison, J. L.

Published in:
Journal of Geophysical Research

DOI:
10.1029/2011JF002154

Publication date:
2012

Melting and refreezing beneath Roi Baudouin Ice Shelf (East Antarctica) inferred from radar, GPS, and ice core data

F. Pattyn,[1] K. Matsuoka,[2] D. Callens,[1] H. Conway,[3] M. Depoorter,[1] D. Docquier,[1] B. Hubbard,[4] D. Samyn,[1,5] and J. L. Tison[1]

Received 14 July 2011; revised 2 September 2012; accepted 5 September 2012; published 11 October 2012.

[1] Ice-penetrating radar profiles across the grounding line of a small ice-rise promontory located within the Roi Baudouin Ice Shelf in the Dronning Maud Land sector of East Antarctica show downward dipping englacial radar-detected reflectors. Model results indicate that this reflector pattern is best fit by including basal melting of at least 15 cm a^{-1}. This rate of melting is low compared with rates observed on larger ice shelves in both West and East Antarctica. Ice cores extracted from a rift system close to the ice-rise promontory show several meters of marine ice accreted beneath the shelf. These observations of low rates of basal melting, and limited distribution of accreted marine ice suggest that either Antarctic surface water may reach the ice shelf base or that circulation beneath the shelf is likely dominated by the production of high salinity shelf water rather than the incursion of circumpolar deep water, implying a weak sub-shelf circulation system here. Many of the ice shelves located along the coast of Dronning Maud Land are, like Roi Baudouin Ice Shelf, characterized by frequent ice rises and promontories. Therefore, it is highly likely that these are also of shallow bathymetry and are subject to similarly weak side-shelf basal melting and refreezing.

Citation: Pattyn, F., K. Matsuoka, D. Callens, H. Conway, M. Depoorter, D. Docquier, B. Hubbard, D. Samyn, and J. L. Tison (2012), Melting and refreezing beneath Roi Baudouin Ice Shelf (East Antarctica) inferred from radar, GPS, and ice core data, *J. Geophys. Res.*, *117*, F04008, doi:10.1029/2011JF002154.

1. Introduction

[2] Marine ice sheets that terminate in the ocean are particularly sensitive to perturbations at the grounding line [*Weertman*, 1974; *Dupont and Alley*, 2005; *Pattyn et al.*, 2006; *Schoof*, 2007; *Gagliardini et al.*, 2010]. Sub-shelf melting occurs near the grounding lines of many of the major outlet glaciers throughout Antarctica [*Rignot and Jacobs*, 2002; *Pritchard et al.*, 2012]. High melt rates underneath ice shelves have been measured in both West Antarctica [*Payne et al.*, 2007; *Thoma et al.*, 2008; *Jenkins et al.*, 2010], and East Antarctica [*Smedsrud et al.*, 2006; *Nicholls et al.*, 2006, 2008]. Observations of synchronous rapid thinning of the floating termini of several glaciers in a region are generally taken to be an indication that the changes are being forced by the ocean [*Shepherd et al.*, 2004; *Thoma et al.*, 2008]. Such forcing leads to increased discharge of inland ice across the grounding line [*Schoof*, 2007; *Rignot et al.*, 2008; *Pritchard et al.*, 2012]. Sub-shelf melting near grounding lines is linked to patterns of large-scale water circulation [*Lewis and Perkins*, 1986; *Jacobs et al.*, 1992; *Holland*, 2008]. Sub-shelf melt rates are relatively high when circumpolar deep water (CDW) reaches the continental shelf, and generally lower when sea ice formation results in high salinity shelf water (HSSW). Melting and freezing along the shelf interface are part of the "ice pump" that is controlled in part by the intensity of HSSW circulation [*Lewis and Perkins*, 1986].

[3] However, the most common water mass over the narrow continental shelves of East Antarctica is the Antarctic Surface Water (ASW) [*Whitworth et al.*, 1998]. At the coast this surface layer deepens as a result of downwelling forced by the easterly winds blowing along the coast. Where the ice sheet topography is steep and the continental shelf narrow (i.e. around East Antarctica) the downwelling is so effective that the whole of the water column over the continental shelf is comprised of ASW [*Nøst et al.*, 2011]. Similar to HSSW,

[1]Laboratoire de Glaciologie, Université Libre de Bruxelles, Brussels, Belgium.
[2]Norwegian Polar Institute, Tromsø, Norway.
[3]Department of Earth and Space Sciences, University of Washington, Seattle, USA.
[4]Centre for Glaciology, Institute of Geography & Earth Sciences, Aberystwyth University, Ceredigion, UK.
[5]Glaciology Research Group, University of Uppsala, Uppsala, Sweden.

Corresponding author: F. Pattyn, Laboratoire de Glaciologie, Université Libre de Bruxelles, Av. F.D. Roosevelt 50, B–1050 Brussels, Belgium. (fpattyn@ulb.ac.be)

0148-0227/12/2011JF002154

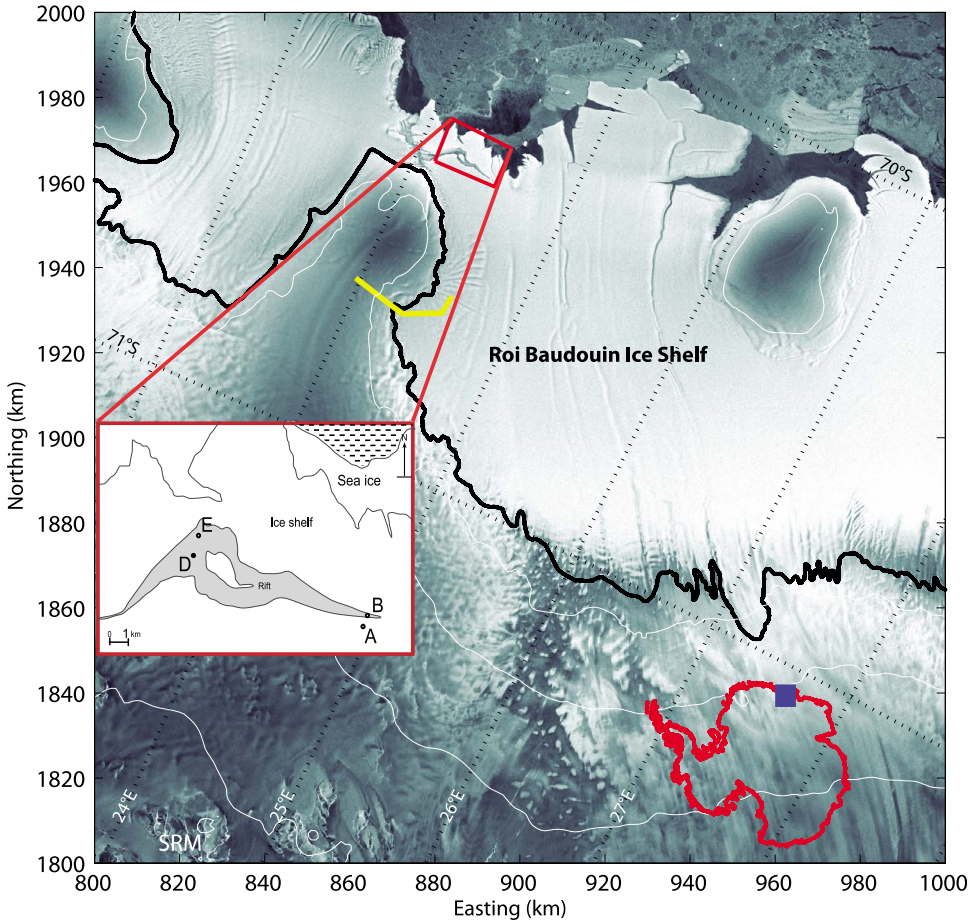

Figure 1. Location of the ice-rise promontory and the Roi Baudouin Ice Shelf (RBIS), Dronning Maud Land, East Antarctica. Contour lines are in white (contour interval is 300 m, starting at 200 m a.s.l.) [*Bamber et al.*, 2009]. The grounding line is given in black [*Bindschadler et al.*, 2011]. The yellow line is the radar traverse. Location of the boreholes in the rift are shown in the inset figure. RAMP (Radarsat) is used as a background image. SRM = Sør Rondane Mountains.

this cold ASW can also melt the ice shelf base [*Hattermann et al.*, 2012], producing Ice Shelf Water (ISW). This ISW, derived from melting meteoric ice and mixing with HSSW/ASW, is also an important component of the ocean circulation. It is known that ISW production varies for different ice shelves but relative contributions from HSSW and CDW are not known for much of East Antarctica.

[4] Most of the evidence for ice-ocean interactions comes from the large Antarctic ice shelves or from ice shelves of the West Antarctic Ice Sheet, but apart from studies on Fimbul ice shelf [*Nicholls et al.*, 2006, 2008; *Hattermann et al.*, 2012], little is known about the ice shelves in the Dronning Maud Land (DML) sector of East Antarctica, although most of the DML coast is characterized by marine-terminating glaciers in ice shelves.

[5] Herein, we combine several empirical lines of evidence to investigate the nature of sub-shelf circulation beneath an ice shelf on the Princess Ragnhild Coast, i.e., Roi Baudouin Ice Shelf (RBIS), DML, East Antarctica. We use ice-penetrating radar, GPS measurements and ice core drilling to investigate ice-ocean interactions on RBIS. Comparison of observed radar-detected englacial reflectors with results from an ice flow model is used to infer basal melting across the grounding line. Direct evidence of sub-shelf marine ice accretion comes from four ice cores drilled through the shelf.

2. Study Area

[6] During the Austral summer 2008–09, we conducted field work in the vicinity of a small ice-rise promontory in RBIS, East Antarctica. Surface topography shows that the ice-rise promontory has a local flow pattern (Figure 1). Downstream of the promontory, a large rift system ~5 km from the ice shelf edge has a maximum width of 2 km and is filled with well consolidated "ice mélange". The bathymetry beneath the ice shelf is relatively shallow; it is 200–300 m b.s.l. near the shelf front [*Nishio et al.*, 1984], and it approaches 500 m b.s.l. near the grounding line [*Nishio et al.*, 1984; *Timmermann et al.*, 2010]. In view of our measured ice thickness, water column thickness beneath the shelf varies between 0 and 200 m. The ice velocity in this area is several tens of meters per year, but reaches values up to 350 m a^{-1} in the central part

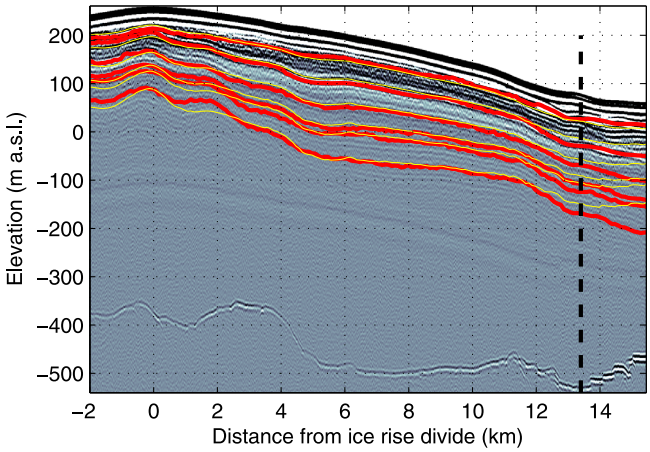

Figure 2. Section of radar profile (location shown in Figure 1) across the ice-rise promontory and the grounding line (vertical dashed line). Comparison of radar-detected reflectors (red), and modeled isochrones (yellow) for the standard experiment (no basal melting) shows large mismatch at the grounding line and within the ice shelf; the mismatches for different model runs are shown in Figure 3.

of RBIS, further to the east of our study area [*Rignot et al.*, 2011].

3. Field Measurements

3.1. Ice-Penetrating Radar and GPS Profiling

[7] We collected ice-penetrating radar profiles across the ice-rise promontory and the ice shelf (Figure 1), using a 5-MHz impulse radar system [*Matsuoka et al.*, 2012]. The transmitter and receiver were separated by 45 m and towed in line. Each record consists of several hundred stacked (averaged) waveforms to improve the signal-to-noise ratio. Additional processing includes bandpass filtering, corrections for surface topography and conversion of two way travel time to depth. We assume the wave speed in ice is 169 m μs^{-1}. Uncertainty in thickness comes from uncertainty in the wave speed (about 2 m μs^{-1}) and from picking the two-way travel time from the surface to the bed. The former corresponds to 1.2% of the ice thickness and the latter is about 0.1 μs for 5 MHz, which corresponds to ~8.5 m. Assuming the errors are uncorrelated, total uncertainty on the ice-rise promontory (<600 m thick) is up to ~11 m. On the ice shelf (~250 m thick), total uncertainty is ~9 m.

[8] Radar profiles show both reflections from the bed and englacial reflectors. Ice thickness is ~600 m between the crest of the ice-rise promontory and the grounding line (Figure 2). Downstream from the grounding line on the ice shelf, ice thickness decreases rapidly to ~250 m. At some locations on the shelf, clutter from multiple hyperbolic echoes beneath surface rumples hampered detection of the basal interface. In previous work we found an abrupt increase in basal reflectivity (near km 13), which is within a kilometer of where the shelf is freely floating [*Matsuoka et al.*, 2012]. The magnitude of this reflectivity change is consistent with a change from a grounded (possibly wet) environment to an ice-ocean interface [*Matsuoka et al.*, 2012].

[9] Profiles were positioned using a roving Leica SR20 differential GPS (L1) referenced to a base station located on the grounded ice-rise promontory. The absolute position of the base station on the ice-rise promontory was obtained from Precise Point Processing, and further adjusted to the EGM96 geoid model to obtain a position relative to mean sea level. The EGM96 model has a discrepancy of 0.27 m compared to measured geoid heights in Breid Bay, near our field site [*Shibuya et al.*, 1999]. A tide model [*Padman et al.*, 2002] was employed to further correct elevations of the roving station on the ice shelf. The tide model predicts tidal amplitudes of less than 1.6 m, with changes of less than 0.4 m predicted over the 5-hour period of our radar and GPS measurements across the ice shelf. Horizontal and vertical position errors for the roving GPS are of the order of 0.1–0.2 m [*Pattyn et al.*, 2010]. For subsequent analyses, we prescribed the grounding line to be the position where the ice becomes freely floating.

3.2. Ice Core Drilling

[10] To determine the presence of marine ice, four ice cores between 10 and 38 m long were drilled north of the ice-rise promontory using either an Eclipse or a SIPRE-based electromechanical drill (The Eclipse drill allows drilling down to several hundred meters, while the SIPRE-type drill is more portable and specially equipped for drilling into water saturated permeable ice, such as ice shelf ice and rift ice would be. Both were used in the field.) (Figure 1): (i) on the ice shelf (core A); (ii) on the slope entering the apex of the rift (core B); (iii) within the rift system (cores D and E). An optical televiewer [*Hubbard et al.*, 2008, 2012] was deployed in each of the boreholes. Core samples were generally analyzed at 0.5–1.0 m depth intervals for their isotopic composition (δ^{18}O, δD), bulk density, salinity and ice texture. Bulk salinity was measured according to standard procedure [*Khazendar et al.*, 2001], with precision of ±0.05 psu. Bulk density was measured with the mass/volume technique (±0.05 precision). Isotopic measurements were made using a Thermo-Finnigan Mass Spectrometer Delta Advantage (δ^{18}O ± 0.05‰, δD ± 1.00‰). On core A, samples of isotopes and density of the meteoric ice collected at 100 mm resolution (not shown) reveal a clear seasonal signal. The accumulation rate (0.27 m a^{-1} w.e.) derived from the measurements is in accordance with regional mass balance modeling results [*van de Berg et al.*, 2006].

4. Ice-Flow Modeling

4.1. Model Setup

[11] Englacial reflectors detected with 5-MHz radar are principally caused by changes in ice density and acidity [*Fujita et al.*, 1999], and they are generally considered to be isochrones. In this section we generate isochrones using a numerical ice flow model and conduct experiments with different boundary conditions to determine the range of conditions that minimize the mismatch between the spatial pattern of modeled and measured reflectors.

[12] In regions where radar-detected reflectors are at shallow depths (and given the low ice flow velocities of the grounded ice sheet) the recent spatial pattern of accumulation can be inferred using the local-layer approximation [*Haefeli*, 1963; *Waddington et al.*, 2007]. We scale the local

accumulation pattern across the ice-rise promontory using the regional value of 0.27 m a^{-1} w.e. [*van de Berg et al.*, 2006].

[13] We use an isothermal higher-order, steady state ice sheet model [*Pattyn*, 2002a, 2010], constrained by the local surface mass balance obtained from the local-layer approximation, to reconstruct the age distribution across the ice-rise promontory and shelf. In a Cartesian coordinate system, the horizontal velocity field along a flowline and under plane strain conditions is [*Pattyn*, 2002a]:

$$4\frac{\partial}{\partial x}\left(\eta\frac{\partial u}{\partial x}\right)+\frac{\partial}{\partial z}\left(\eta\frac{\partial u}{\partial z}\right)=\rho g\frac{\partial(b+H)}{\partial x}, \tag{1}$$

where u is the horizontal velocity along the flowline, b and H the bottom of the ice and the ice thickness, respectively, and where the effective viscosity η is defined by

$$\eta=\frac{1}{2}A^{-1/n}\left[\left(\frac{\partial u}{\partial x}\right)^2+\frac{1}{4}\left(\frac{\partial u}{\partial z}\right)^2\right]^{(1-n)/2n}. \tag{2}$$

Here, A and n are the flow parameter and the exponent in Glen's flow law, respectively ($A = 10^{-17}$ Pa^{-n} a^{-1}; $n = 3$). The value of A corresponds to ice with a mean temperature of -10°C, which is consistent with the balance velocities imposed at the boundaries of the domain (see below). At this point, thermomechanical coupling is not considered; the effect of including this coupling on the modeled spatial pattern of isochrones would influence the absolute age of the lower layers, where the highest temperature gradients occur. However, since detected reflectors are restricted to the upper half of the ice column, this effect is therefore limited.

[14] For modeling purposes it is convenient to scale the velocity field in the vertical dimension to the ice thickness. Defining $\zeta = (b + H - z) / H$, the surface transforms to $\zeta = 0$, while the bottom of the ice mass becomes $\zeta = 1$. The horizontal flow field (1) is therefore rewritten as [*Pattyn*, 2003]:

$$4\frac{\partial}{\partial x}\left(\eta\frac{\partial u}{\partial x}+a_x\eta\frac{\partial u}{\partial\zeta}\right)+4a_x\frac{\partial}{\partial\zeta}\left(\eta\frac{\partial u}{\partial x}+a_x\eta\frac{\partial u}{\partial\zeta}\right)+\frac{1}{H^2}\frac{\partial}{\partial\zeta}\left(\eta\frac{\partial u}{\partial\zeta}\right)=\rho g\frac{\partial(b+H)}{\partial x}, \tag{3}$$

where

$$a_x=\frac{1}{H}\left(\frac{\partial b}{\partial x}+(1-\zeta)\frac{\partial H}{\partial x}\right), \tag{4}$$

while (2) transforms to

$$\eta=\frac{1}{2}A^{-1/n}\left[\left(\frac{\partial u}{\partial x}+a_x\frac{\partial u}{\partial\zeta}\right)^2+\frac{1}{4H^2}\left(\frac{\partial u}{\partial\zeta}\right)^2\right]^{(1-n)/2n}. \tag{5}$$

Boundary conditions for the model are obtained from balance velocities derived by integrating the surface mass balance from the ice divide to the end of the surveyed profile. The velocity at the model domain boundary is then fixed to the balance velocity. Basal velocities are kept zero at the base, except in the ice shelf, where basal friction is set to zero so that velocities at the base equal those at the surface [*Pattyn*, 2003].

[15] The vertical velocity field is derived from mass conservation combined with the incompressibility condition for ice. Given an ice sheet in steady state, a simple analytical expression can be obtained, based on the horizontal velocity field [*Hindmarsh*, 1999], i.e.

$$w(x,\zeta)=-\left[\frac{\zeta^{n+2}-1+(n+2)(1-\zeta)}{n+1}\right]\dot{a}-\dot{m}+u\nabla b+(1-\zeta)u\nabla H, \tag{6}$$

where w is the vertical velocity, $\dot{a}$ is the local accumulation rate, and $\dot{m}$ is the basal melting rate. For plug flow (ice shelf), (6) reduces to $w(x,\zeta) = (\zeta - 1)\dot{a} - \zeta\dot{m}$ [*Hindmarsh*, 1999].

[16] The age calculation within the ice sheet is written as an advection equation with a small diffusion term added in order to stabilize the numerical solution [*Huybrechts*, 1994; *Greve*, 1997; *Pattyn*, 2002b]:

$$\frac{\partial\mathcal{A}}{\partial t}=1-u\frac{\partial\mathcal{A}}{\partial x}-w\frac{\partial\mathcal{A}}{\partial z}+D_a\frac{\partial^2\mathcal{A}}{\partial z^2} \tag{7}$$

where $\mathcal{A}$ is the ice age (a), and D_a a diffusion coefficient (5×10^{-8} m^2 a^{-1}) [*Mügge et al.*, 1999]. Written in the scaled coordinate system, (7) becomes

$$\frac{\partial\mathcal{A}}{\partial t}=1-u\frac{\partial\mathcal{A}}{\partial x}+\left(\frac{w}{H}-a_x\right)\frac{\partial\mathcal{A}}{\partial\zeta}+\frac{D_a}{H^2}\frac{\partial^2\mathcal{A}}{\partial\zeta^2}. \tag{8}$$

Boundary conditions to this equation are $\mathcal{A}(0) = 0$ at the surface and the age of the integration time at the bottom of the ice mass (typically 10 ka). The choice of this value has no effect on the age of the identified isochrones. The model is solved numerically on a finite difference grid, equally spaced in x and unequally spaced in ζ, providing a higher resolution approaching the base of the ice mass [*Pattyn*, 2002a].

4.2. Replicating Englacial Radar Reflectors

[17] Based on the inferred accumulation pattern from the shallow radar reflectors, each observed isochrone was dated using a minimization procedure by reducing the mismatch between observed and modeled isochrone depth, leading to ages ranging from 175 to 957 a BP for the uppermost and lowermost isochrones, respectively. This procedure consists of calculating the misfit between an observed isochrone and a series of modeled isochrones of different age. The smallest misfit then corresponds to the age of the observed isochrone. In general, the model produces a good fit between observed and calculated isochrone depths for the grounded ice sheet profile, except for the area around the grounding line where radar-detected reflectors dip downward (Figure 2).

4.3. Causes of Downwarped Reflectors Near the Grounding Line

[18] This anomaly could be caused by several processes, including subglacial melting at the grounding line or a local increase in surface accumulation, both of which could cause downward motion of the reflectors. Other possible processes could be related to temporal variability in surface accumulation (unlikely since the grounded part would be equally affected by this effect), or to the convergent flow as the

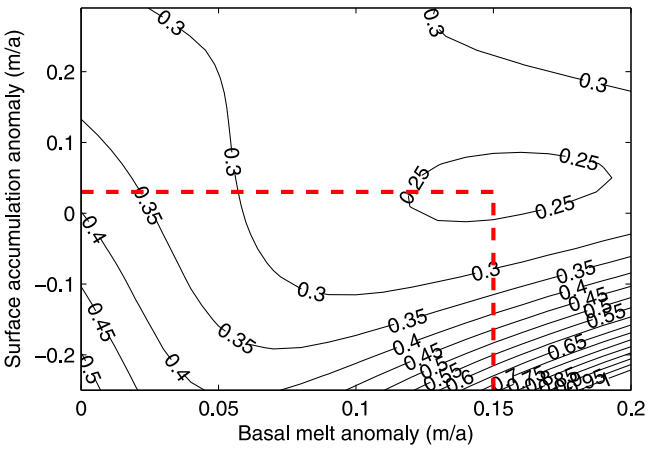

Figure 3. Minimization of the RMS error (m) between observed and modeled isochrones for different combinations of accumulation/ablation and basal melting near the grounding line. The best fit is obtained with basal melting of 15 cm a^{-1} and no accumulation anomaly.

flowline turns into the main ice shelf (three-dimensional effects, Figure 1). These are discussed below.

[19] In order to examine possible effects from sub-shelf melting and surface accumulation, we follow the approach of others [e.g., *Catania et al.*, 2006, 2010] and conduct a series of sensitivity experiments using the ice-flow model. We forced the model with anomalies in surface accumulation/ablation (ranging from −0.25 to 0.25 m a^{-1}) and basal melting (0 to 0.25 m a^{-1}) for the ice shelf (between the grounding line and a distance of 2 km downstream) and calculated the RMS error between observed and calculated isochrone depths (Figure 3). For each experiment shown, we assume that the basal melting and accumulation anomalies are constant through time and spatially distributed over a zone of 2 km. The best fit to the data is obtained with no surface accumulation anomaly and basal melting of 0.15 m a^{-1} (Figure 3). Reasonable fits can be obtained with small surface anomalies and slightly lower or higher values of basal melting (0.1 to 0.2 m a^{-1}), but all results indicate that basal melting is required.

[20] The experiments above consider a continuously applied anomaly over a sustained period of time. We therefore tested applying anomalies over shorter time spans as well, but all led to worse misfits. Due to horizontal ice flow, any anomaly is advected downstream, hence the upwarping of the deeper layers at and downstream from the grounding line disappears when the anomaly is applied for any given period in the past.

[21] Conditions of plane strain are valid for the grounded ice flow in the saddle area of the ice-rise promontory (where flowlines are strictly parallel to each other), but do not apply in the ice shelf because of the turning of ice flow (indicated by the flow stripes evident on the ice shelf, Figure 1). In this area, ice flows convergently. Since mass conservation implies that $\nabla \dot{\mathbf{v}} = 0$, we obtain for a flowline [*Reeh*, 1988; *Pattyn*, 2002a]:

$$\frac{\partial w}{\partial \zeta} = H\left(\frac{\partial u}{\partial x} + a_x \frac{\partial u}{\partial \zeta}\right) + H\dot{\varepsilon}_{yy}, \tag{9}$$

where $\dot{\varepsilon}_{yy} = \partial v/\partial y$ is the transverse strain rate and v the velocity in the y direction. Plug flow of the ice shelf implies that $\partial w/\partial \zeta = \dot{a} - \dot{m}$ and that $\partial u / \partial \zeta = 0$. Under simplified conditions of plane strain, $\dot{\varepsilon}_{yy} = 0$, it is therefore safe to say that

$$H\frac{\partial u}{\partial x} = \dot{a} - \dot{m}. \tag{10}$$

However, for convergent flow, $\dot{\varepsilon}_{yy} < 0$, so the vertical velocity gradient $\partial w / \partial \zeta$ is reduced. Since $\partial w/\partial \zeta - \dot{a} = -\dot{m}$, this implies a higher basal melt rate to match the downwarping pattern than that calculated above. Conversely, divergent flow would have the opposite effect (i.e., less basal melt needed to explain the pattern). Although it is difficult to estimate the amount of buttressing due to the convergent flow, we can consider the calculated basal melt anomaly of 0.15 m a^{-1} is a lower bound and actual melt rates are likely higher.

5. Sub-shelf Accretion of Marine Ice

[22] Sub-shelf melting at the grounding line can result in accretion of marine ice beneath the shelf caused by consolidation of frazil ice that originates in supercooled water. $\delta^{18}O$ values for marine ice are close to +2‰, proving that it originated from freezing seawater [*Gow and Epstein*, 1972; *Morgan*, 1972; *Oerter et al.*, 1992]. Bulk salinity of consolidated marine ice at depth varies between 0.03 and 0.3 psu, which is two or three orders of magnitude higher than meteoric ice and one or two orders of magnitude lower than sea ice [*Souchez et al.*, 1991; *Tison et al.*, 1993; *Khazendar et al.*, 2001; *Tison and Khazendar*, 2001].

[23] In principle, the thickness of a marine ice layer beneath an ice shelf that is in hydrostatic equilibrium could be determined by comparing the measured surface elevation of the floating shelf with the surface elevation calculated from buoyancy [*Corr et al.*, 1995; *Fricker et al.*, 2001]. In practice, the calculation is hampered by large uncertainty in the density profile through the shelf, and uncertainties and ambiguities in the radar-detected ice thickness (Section 3.1). Our measurements of temperature, bulk salinity, ice texture, and stable isotopes from the ice cores (Figure 4) offer another way to investigate marine ice accretion.

[24] Firn and meteoric ice in the region have negative $\delta^{18}O$ values (mean = −21.5 ± 2.2‰), negligible (below detection limits) salinity, and a polygonal granular texture. When soaked with seawater (as seen in the lower section of Core B, Figure 4), the ice temperature increases to the freezing point of seawater (−1.9°C), causing crystals to become more rounded. Bulk salinity also increases (typically to 0.3–2 psu) in this facies, as does $\delta^{18}O$, indicating mixing between meteoric ice crystals and frozen seawater.

[25] The contribution from firn to the "ice mélange" decreases westward within the rift zone. Core D shows a transition below ~5 m with a sharp increase in $\delta^{18}O$ (becoming less negative), and slowly increasing salinities, down to 8–9 m depth (Figure 4). This transition zone could be caused by recrystallized soaked firn, or by snow ice (top layer of sea ice formed by flooding of the snow). The lower 10 m section shows a granular texture with constant positive $\delta^{18}O$ values and salinities ranging from 1 to 9, which is more typical of sea ice rather than marine ice. It is however highly unlikely that granular frazil sea ice (typically formed under conditions of

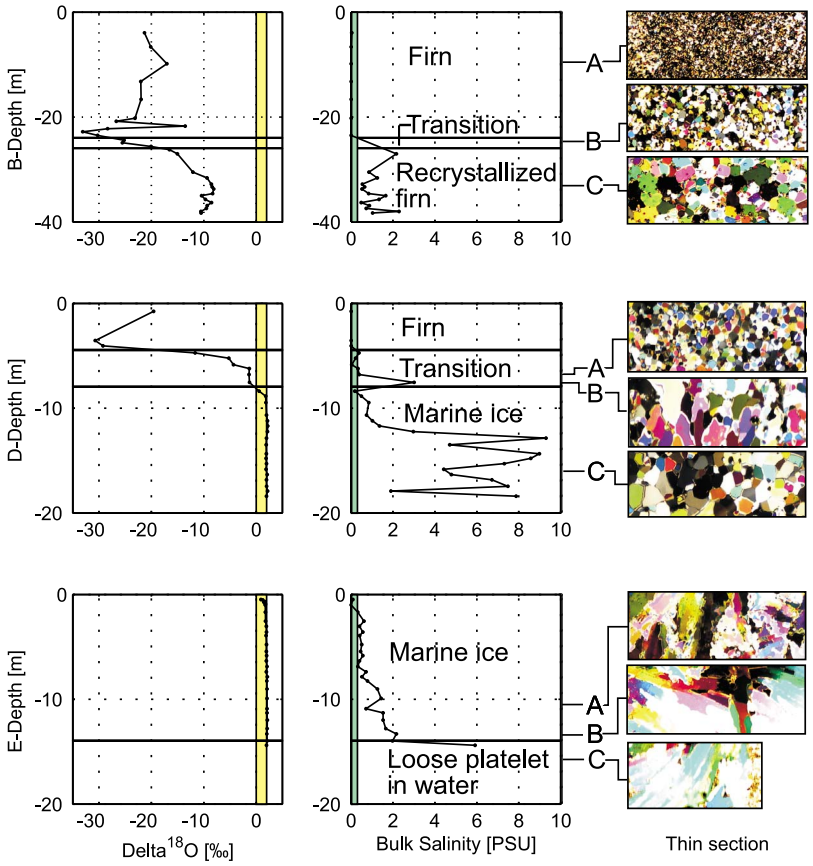

Figure 4. Isotopic composition, bulk salinity and texture for Cores B, D, and E drilled in the rift. The yellow and green bands show the reported ranges of $\delta^{18}O$ and bulk salinity for marine ice, i.e., 0–2‰ and 0.03–0.3 psu, respectively. Long axis side of thin sections is 4.5 cm. See Figure 1 for location of the drill sites.

turbulent winds) could accumulate to a total thickness of nearly 10 m. Under a turbulent regime, granular sea ice is quickly formed but can never attain depths of several meters, as the turbulence has no effect anymore once sea ice cover is sufficiently thick. In that case, columnar sea ice is more likely to form [*Martin*, 1981]. We therefore favor a marine ice origin, for the lower section of the core, with recent consolidation in near-surface conditions explaining the higher salinity [*Tison et al.*, 1998].

[26] Core E (Figure 4) is characterized by the absence of any snow/firn and shows ~12 m of marine ice outcropping at the surface in association with a dense network of crevasse fills. It also shows a regular increase of the salinity in the lower, younger layers. A profile with the televiewer showed several meters of loose frazil ice platelets in the sub-shelf water [*Hubbard et al.*, 2012]. This configuration is similar to that described by [*Tison et al.*, 1998] at the front of Hells Gate Ice Shelf, Antarctica, where the strong contrast in marine ice texture (granular as opposed to banded; the equivalent to facies at the bottom of core D as opposed to core E in the present case) was attributed to water circulation below the shelf.

6. Discussion

[27] Most observations of melt rates underneath ice shelves stem from satellite altimetry [e.g., *Pritchard et al.*, 2012]. However, close to the grounding line where the ice shelf is not freely floating, ice thickness may well be overestimated using the satellite technique, leading to biases in basal melt rates. Our estimates based on measured ice thickness are not hampered by this bias and therefore more reliable and robust.

[28] It is generally thought that high rates of sub-shelf melting such as those observed on the Pine Island shelf (20–30 m a^{-1}) [*Rignot*, 1998; *Jacobs et al.*, 2011], and George VI Ice Shelf (2.2–2.8 m a^{-1}) [*Potter and Paren*, 1985; *Corr et al.*, 2002] are caused by incursions of CDW through deep troughs crossing the continental shelf and entering ice shelf cavities. More modest melting (~0.6 m a^{-1}) measured beneath the Filchner Ice Shelf has been attributed to a convective thermohaline circulation due to HSSW formation [*Hellmer and Olbers*, 1989; *Nicholls et al.*, 2006]. Similar melt rates of 0.85 (but up to 2.85) m a^{-1} have been measured using phase-sensitive radar near the grounding line of Rutford Ice Stream [*Jenkins et al.*, 2006], and melt rates up to 0.85 m a^{-1} were also measured near the shore of the Fimbul ice shelf [*Nicholls et al.*, 2006, 2008].

[29] In contrast, our measurements across the grounding line of Roi Baudouin Ice Shelf indicate relatively small melt rates (~0.15 m a^{-1}) compared with those measured beneath large ice shelves. Tidal influences can increase the intensification of sub-shelf circulation, resulting in increased melting and refreezing [*MacAyeal*, 1984; *Makinson et al.*, 2011]. Local geometry of the water column beneath a shelf and tidal mixing may also be important; model simulations [*Holland*,

2008] show that such mixing is confined to small areas and may only become significant under near-freezing conditions where the ocean cavity slope is shallow and tidal stirring is vigorous. Although such favorable conditions do exist beneath Roi Baudouin Ice Shelf, the relatively low melt rate indicated by our model-based interpretations of the radar data (Figure 3) suggests that this mechanism is not strong.

[30] Our observations indicate that the occurrence of accreted marine ice is restricted primarily to the rift zone. In such areas, it is thought that melt-driven convection at the sides of a rift cause cavity water to ascend and supercool, resulting in marine ice formation [*Khazendar and Jenkins*, 2003]. *Khazendar* [2000] has also shown that the amount of ice accreted in such rifts is greatly increased by the presence of pre-existing ISW formed upstream. Moreover, some preliminary conductivity/temperature/depth profiles collected from boreholes near the edge of the shelf, downstream from the rift suggest that a weak outflow of shallow ISW is present.

[31] The weak melting at the grounding line implies a weak buoyancy-forced circulation and correspondingly low freezing rates (i.e. a weak "ice pump"). Also the ice front region could easily be influenced by downwelling of the seasonally warmer surface layer [*Hattermann et al.*, 2012]. Even if all the cavity waters were all at the surface freezing point, basal freezing may only influence the outer part of the ice shelf near the ice front [*Lane-Serff*, 1995], and marine ice could be melted off by downwelling beneath the ice front, leaving only marine ice in the rifts where it is protected.

[32] The incursion of HSSW or the downwelling of the seasonally warmer surface layer rather than CDW beneath RBIS is most probably controlled by regional water mass flows combined with RBIS' shallow sub-shelf cavity. Since other ice shelves in the sector appear to be underlain by similarly shallow cavities, as evidenced by shelf-edge bathymetric data and the presence of frequent ice rises along the Princess Ragnhild Coast, it is likely that similar conditions might well prevail more widely than at RBIS alone [e.g., *Hattermann et al.*, 2012]. Thus, we postulate that many of the ice shelves in this sector of East Antarctica are characterized by sub-shelf water circulation systems that are dominated by either the incursion of HSSW or the downwelling of ASW and characterized by low levels of sub-shelf melting and freezing relative to larger shelf systems located elsewhere in Antarctica. However, this inference has yet to be tested directly and might be considered a priority for future investigations. Nevertheless, the shallowness of the bathymetry in this area is restricted to the sections close to ice rises and ice-rise promontories. Deeper troughs at the exit of large outlet glaciers feeding into RBIS and other ice shelves in this sector of DML do exist and may eventually exhibit a different type of ice/ocean interaction.

7. Conclusions

[33] Ice-penetrating radar and kinematic GPS surveys across a grounding line, and ice core drilling within a zone of rifting farther downstream reveal sub-ice shelf melting near the grounding line and limited accretion of marine ice in the rift zone. The rate of sub-ice shelf melting is 0.15 m a^{-1}, which is rather low for an Antarctic ice shelf. Marine ice accretion is found in a rift system close to the edge of the ice shelf where it is either formed locally or protected from melting due to warmer surface waters near the shelf edge. We conclude that the weak melt rates at the grounding line are not sufficient to sustain large-scale accretion of marine ice. We suspect that similar weak melting/refreezing conditions occur along much of the coastal sector in Dronning Maud Land where ice shelves are interspersed by ice rises and where rifting commonly occurs between those ice rises and the shelf front.

[34] **Acknowledgments.** This paper forms a contribution to the Belgian Research Programme on the Antarctic (Belgian Federal Science Policy Office), Project EA/11/3A 'Belgian Ice Sheet – Shelf Ice Measurements in Antarctica (BELISSIMA)'. K.M. and H.C. were partly supported by a University of Washington Royalty Research Fund (project 4208). D.C. is supported by a FRIA (FRS–FNRS) grant. The isotopic analyses were carried out by B. Stenni at the Isotope Geochemistry Laboratory of the University of Trieste (Italy). The authors are indebted to A. Hubert, R. Wagemans and K. Soete for their valuable assistance in the field. We thank M. Truffer, M. Koutnik and the other referees for their constructive comments on the original manuscript.

References

Bamber, J. L., J. L. Gomez-Dans, and J. A. Griggs (2009), A new 1 km digital elevation model of the antarctic derived from combined satellite radar and laser data—Part 1: Data and methods, *Cryosphere*, *3*(1), 101–111.

Bindschadler, R. A., H. Choi, and ASAID Collaborators (2011), High-Resolution Image-derived Grounding and Hydrostatic Lines for the Antarctic Ice Sheet, http://nsidc.org/data/docs/agdc/nsidc0489_bindschadler/index.html, Natl. Snow and Ice Data Cent., Boulder, Colo.

Catania, G. A., H. Conway, C. F. Raymond, and T. A. Scambos (2006), Evidence for floatation or near floatation in the mouth of Kamb Ice Stream, West Antarctica, prior to stagnation, *J. Geophys. Res.*, *111*, F01005, doi:10.1029/2005JF000355.

Catania, G. A., C. Hulbe, and H. Conway (2010), Grounding line basal melt rates from radar-derived internal stratigraphy, *J. Glaciol.*, *56*(197), 545–554.

Corr, H., M. Popple, and A. Robinson (1995), Airborne radio echo investigations of a marine ice body, *Filchner-Ronne Ice Shelf Progr. Rep. 8*, pp. 14–17, Alfred Wegener Inst. for Polar and Mar. Res., Bremerhaven, Germany.

Corr, H. F. J., A. Jenkins, K. W. Nicholls, and C. S. M. Doake (2002), Precise measurement of changes in ice-shelf thickness by phase-sensitive radar to determine basal melt rates, *Geophys. Res. Lett.*, *29*(8), 1232, doi:10.1029/2001GL014618.

Dupont, T. K., and R. B. Alley (2005), Assessment of the importance of ice-shelf buttressing to ice-sheet flow, *Geophys. Res. Lett.*, *32*, L04503, doi:10.1029/2004GL022024.

Fricker, H. A., S. Popov, I. Allison, and N. Young (2001), Distribution of marine ice beneath the Amery Ice Shelf, *Geophys. Res. Lett.*, *28*(11), 2241–2244.

Fujita, S., H. Maeno, S. Uratsuka, T. Furukawa, S. Mae, Y. Fujii, and O. Watanabe (1999), Nature of radio echo layering in the Antarctic ice sheet detected by a two-frequency experiment, *J. Geophys. Res.*, *104*(B6), 13,013–13,024.

Gagliardini, O., G. Durand, T. Zwinger, R. C. A. Hindmarsh, and E. L. Meur (2010), Coupling of ice-shelf melting and buttressing is a key process in ice-sheet dynamics, *Geophys. Res. Lett.*, *37*, L14501, doi:10.1029/2010GL043334.

Gow, A. J., and S. Epstein (1972), On the yse of stable isotopes to trace the origins of ice in a floating ice tongue, *J. Geophys. Res.*, *77*(33), 6552–6557.

Greve, R. (1997), Large-scale ice-sheet modelling as a means of dating deep ice cores in Greenland, *J. Glaciol.*, *43*(144), 307–310.

Haefeli, R. (1963), A numerical and experimental method for determining ice motion in the central parts of ice sheets, *IAHS Publ.*, *61*, 253–260.

Hattermann, T., O. A. Nøst, J. M. Lilly, and L. H. Smedsrud (2012), Two years of oceanic observations below the Fimbul Ice Shelf, Antarctica, *Geophys. Res. Lett.*, *39*, L12605, doi:10.1029/2012GL051012.

Hellmer, H. H., and D. J. Olbers (1989), On the thermohaline circulation beneath the Filchner-Ronne ice shelves, *Antarct. Sci.*, *3*(4), 433–442.

Hindmarsh, R. C. A. (1999), On the numerical computation of temperature in an ice sheet, *J. Glaciol.*, *45*(151), 568–574.

Holland, P. R. (2008), A model of tidally dominated ocean processes near ice shelf grounding lines, *J. Geophys. Res.*, *113*, C11002, doi:10.1029/2007JC004576.

Hubbard, B., S. Roberson, D. Samyn, and D. Merton-Lyn (2008), Digital optical televiewing of ice boreholes, *J. Glaciol.*, *54*(188), 823–830.
Hubbard, B., J. L. Tison, F. Pattyn, M. Dierckx, T. Boereboom, and D. Samyn (2012), Optical televiewer-based identification and characterization of material facies associated with an Antarctic ice-shelf rift, *Ann. Glaciol.*, *53*(60), 137–146.
Huybrechts, P. (1994), Formation and disintegration of the Antarctic ice sheet, *Ann. Glaciol.*, *20*, 336–340.
Jacobs, S. S., H. H. Helmer, C. S. M. Doake, A. Jenkins, and R. M. Frolich (1992), Melting of ice shelves and the mass balance of Antarctica, *J. Glaciol.*, *38*(130), 357–387.
Jacobs, S. S., A. Jenkins, C. F. Giulivi, and P. Dutrieux (2011), Stronger ocean circulation and increased melting under Pine Island Glacier ice shelf, *Nat. Geosci.*, *4*, 519–523.
Jenkins, A., H. F. J. Corr, K. W. Nicholls, C. L. Stewart, and C. S. M. Doake (2006), Interactions between ice and ocean observed with phase-sensitive radar near an Antarctic ice-shelf grounding line, *J. Glaciol.*, *52*(178), 325–346.
Jenkins, A., P. Dutrieux, S. Jacobs, S. McPhail, J. Perrett, A. Webb, and D. White (2010), Observations beneath Pine Island Glacier in West Antarctica and implications for its retreat, *Nat. Geosci.*, *3*(7), 468–472.
Khazendar, A. (2000), Marine ice formation in rifts of Antarctic ice shelves: A combined laboratory and modeling approach, PhD thesis, Univ. libre de Bruxelles, Brussels.
Khazendar, A., and A. Jenkins (2003), A model of marine ice formation within Antarctic ice shelf rifts, *J. Geophys. Res.*, *108*(C7), 3235, doi:10.1029/2002JC001673.
Khazendar, A., J. L. Tison, B. Stenni, M. Dini, and A. Bondesan (2001), Significant marine-ice accumulation in the ablation zone beneath an Antarctic ice shelf, *J. Glaciol.*, *47*(158), 359–368.
Lane-Serff, G. F. (1995), On meltwater under ice shelves, *J. Geophys. Res.*, *100*(C4), 6961–6965.
Lewis, E. L., and R. G. Perkins (1986), Ice pumps and their rates, *J. Geophys. Res.*, *91*(C10), 11,756–11,762.
MacAyeal, D. R. (1984), Thermohaline circulation below the Ross Ice Shelf: A consequence of tidally induced vertical mixing and basal melting, *J. Geophys. Res.*, *89*(C1), 597–606.
Makinson, K., P. R. Holland, A. Jenkins, K. W. Nicholls, and D. M. Holland (2011), Influence of tides on melting and freezing beneath Filchner-Ronne Ice Shelf, Antarctica, *Geophys. Res. Lett.*, *38*, L06601, doi:10.1029/2010GL046462.
Martin, S. (1981), Frazil ice in rivers and oceans, *Ann. Rev. Fluid Mech.*, *13*, 379–397.
Matsuoka, K., F. Pattyn, D. Callens, and H. Conway (2012), Radar characteristics of the basal interface across the grounding zone of an ice-rise promontory, East Antarctica, *Ann. Glaciol.*, *53*(60), 29–34.
Morgan, V. (1972), Oxygen isotope evidence for bottom freezing on the Amery Ice Shelf, *Nature*, *238*, 393–394.
Mügge, B., A. A. Savvin, R. Calov, and R. Greve (1999), Numerical age computation of the Antarctic ice sheet for dating deep ice cores, in *Advances in Cold-Region Thermal Engineering and Sciences*, edited by Y. W. K. Hutter and H. Beer, pp. 307–318, Springer, New York.
Nicholls, K. W., et al. (2006), Measurements beneath an Antarctic ice shelf using an autonomous underwater vehicle, *Geophys. Res. Lett.*, *33*, L08612, doi:10.1029/2006GL025998.
Nicholls, K. W., E. P. Abrahamsen, K. J. Heywood, K. Stansfield, and S. Osterhus (2008), High-latitude oceanography using the Autosub autonomous underwater vehicle, *Limnol. Oceanogr.*, *53*(5), 2309–2320.
Nishio, F., M. Ishikawa, H. Ohmae, S. Takahashi, and T. Katsushima (1984), A preliminary study of glacial geomorphology in area between Breid Bay and the Sør Rondane Mountains in Queen Maud Land, East Antarctica, *Nankyoku Shiryô*, *83*, 11–28.
Nøst, O. A., M. Biuw, V. Tverberg, C. Lydersen, T. Hattermann, Q. Zhou, L. H. Smedsrud, and K. M. Kovacs (2011), Eddy overturning of the Antarctic Slope Front controls glacial melting in the Eastern Weddell Sea, *J. Geophys. Res.*, *116*, C11014, doi:10.1029/2011JC006965.
Oerter, H., J. Kipfsthül, J. Determann, H. Miller, D. Wagenbach, A. Minikin, and W. Graf (1992), Evidence for basal marine ice in the Filchner-Ronne Ice Shelf, *Nature*, *358*, 399–401.
Padman, L., H. A. Fricker, R. Coleman, S. Howard, and L. Erofeeva (2002), A new tide model for the Antarctic ice shelves and seas, *Ann. Glaciol.*, *34*(1), 247–254.
Pattyn, F. (2002a), Transient glacier response with a higher-order numerical ice-flow model, *J. Glaciol.*, *48*(162), 467–477.
Pattyn, F. (2002b), Ice-flow characteristics over a rough bedrock: Implications for ice-core interpretation, *Polar Meteorol. Glaciol.*, *16*, 42–52.
Pattyn, F. (2003), A new 3D higher-order thermomechanical ice-sheet model: Basic sensitivity, ice-stream development and ice flow across subglacial lakes, *J. Geophys. Res.*, *108*(B8), 2382, doi:10.1029/2002JB002329.
Pattyn, F. (2010), Antarctic subglacial conditions inferred from a hybrid ice sheet/ice stream model, *Earth Planet. Sci. Lett.*, *295*, 451–461.
Pattyn, F., A. Huyghe, S. De Brabander, and B. De Smedt (2006), Role of transition zones in marine ice sheet dynamics, *J. Geophys. Res.*, *111*, F02004, doi:10.1029/2005JF000394.
Pattyn, F., K. Matsuoka, and J. Berte (2010), Glacio-meteorological conditions in the vicinity of the Belgian Princess Elisabeth Station, Antarctica, *Antarct. Sci.*, *22*(1), 79–85.
Payne, A. J., P. R. Holland, A. P. Shepherd, I. C. Rutt, A. Jenkins, and I. Joughin (2007), Numerical modeling of ocean-ice interactions under Pine Island Bay's ice shelf, *J. Geophys. Res.*, *112*, C10019, doi:10.1029/2006JC003733.
Potter, J. R., and J. G. Paren (1985), Interaction between ice shelf and ocean in George VI Sound, Antarctica, in *Antarctica, in Oceanology of the Antarctic Continental Shelf*, *Antarct. Res. Ser.*, vol. 43, edited by S. Jacobs, pp. 35–58, AGU, Washington, D. C., doi:10.1029/AR043p0035.
Pritchard, H. D., S. R. M. Ligtenberg, H. A. Fricker, D. G. Vaughan, M. R. van den Broeke, and L. Padman (2012), Antarctic ice-sheet loss driven by basal melting of ice shelves, *Nature*, *484*, 502–505, doi:10.1038/nature10968.
Reeh, N. (1988), A flow-line model for calculating the surface profile and the velocity, strain-rate, and stress fields in an ice sheet, *J. Glaciol.*, *34*(116), 46–54.
Rignot, E. J. (1998), Fast recession of a West Antarctic glacier, *Science*, *281*(5376), 549–551, doi:10.1126/science.281.5376.549.
Rignot, E. J., and S. S. Jacobs (2002), Rapid bottom melting widespread near Antarctic ice sheet grounding lines, *Science*, *296*(5575), 2020–2023.
Rignot, E. J., J. L. Bamber, M. R. van den Broeke, C. Davis, Y. Li, W. J. van de Berg, and E. van Meijgaard (2008), Recent Antarctic ice mass loss from radar interferometry and regional climate modelling, *Nat. Geosci.*, *1*, 106–110.
Rignot, E., J. Mouginot, and B. Scheuchl (2011), Ice flow of the Antarctic Ice Sheet, *Science*, *333*(6048), 1427–1430, doi:10.1126/science.1208336.
Schoof, C. (2007), Ice sheet grounding line dynamics: Steady states, stability and hysteresis, *J. Geophys. Res.*, *112*, F03S28, doi:10.1029/2006JF000664.
Shepherd, A., D. Wingham, and E. Rignot (2004), Warm ocean is eroding West Antarctic Ice Sheet, *Geophys. Res. Lett.*, *31*, L23402, doi:10.1029/2004GL021106.
Shibuya, K., K. Doi, and S. Aoki (1999), Precise determination of geoid height and free-air gravity anomaly at Syowa Station, Antarctica, *Earth Planets Space*, *51*, 159–168.
Smedsrud, L., A. Jenkins, D. M. Holland, and O. A. Nøst (2006), Modeling ocean processes below the Fimbul Ice Shelf, *J. Geophys. Res.*, *111*, C01007, doi:10.1029/2005JC002915.
Souchez, R., M. Meneghel, J. L. Tison, R. Lorrain, D. Ronveaux, C. Baroni, A. Lozei, I. Tobacco, and J. Jouzel (1991), Ice composition evidence of marine ice transfer along the bottom of a small ice shelf, *Geophys. Res. Lett.*, *18*(5), 849–852.
Thoma, M., A. Jenkins, D. Holland, and S. Jacobs (2008), Modelling circumpolar deep water intrusions on the Amundsen Sea continental shelf, Antarctica, *Geophys. Res. Lett.*, *35*, L18602, doi:10.1029/2008GL034939.
Timmermann, R., et al. (2010), A consistent dataset of Antarctic ice sheet topography, cavity geometry, and global bathymetry, *Earth Syst. Sci. Data*, *3*(2), 231–257, doi:10.5194/essdd-3-231-2010.
Tison, J. L., and A. Khazendar (2001), The isotope/salinity relationship in marine ice: New perspectives, *J. Geophys. Res.*, *106*(C12), 31,387–31,401.
Tison, J. L., D. Ronveaux, and R. Lorrain (1993), Low salinity frazil ice generation at the base of a small Antarctic ice shelf, *Antarct. Sci.*, *5*(3), 309–322.
Tison, J. L., R. Lorrain, A. Bouzette, M. Dini, T. Bondesan, and M. Stiévenard (1998), Linking land fast sea ice variability to marine ice accretion at Hells Gate Ice Shelf, Ross Sea, in *Antarctic Sea Ice Physical Processes, Interactions and Variability*, *Antarct. Res. Ser.*, vol. 74, edited by M. Jeffries, pp. 375–407, AGU, Washington, D. C., doi:10.1029/AR074p0375.
van de Berg, W. J., M. R. van den Broeke, C. H. Reijmer, and E. van Meijgaard (2006), Reassessment of the Antarctic surface mass balance using calibrated output of a regional atmospheric climate model, *J. Geophys. Res.*, *111*, D11104, doi:10.1029/2005JD006495.
Waddington, E. D., T. A. Neumann, M. R. Koutnik, H. P. Marshall, and D. L. Morse (2007), Inference of accumulation-rate patterns from deep layers in glaciers and ice sheets, *J. Glaciol.*, *53*(183), 694–712.
Weertman, J. (1974), Stability of the junction of an ice sheet and an ice shelf, *J. Glaciol.*, *13*, 3–11.
Whitworth, T., A. H. Orsi, S. J. Kim, W. D. Nowlin, and R. A. Locarnini (1998), Water masses and mixing near the Antarctic slope front, in *Ocean, Ice, and Atmosphere: Interactions at the Antarctic Continental Margin*, *Antarct. Res. Ser.*, vol. 75, edited by S. S. Jacobs and R. F. Weiss, pp. 1–27, AGU, Washington D.C., doi:10.1029/AR075p0001.